Single-shot 3D imaging of hydroxyl radicals in the vicinity of a gliding arc discharge

Bao, Yupan; Dorozynska, Karolina; Stamatoglou, Panagiota; Kong, Chengdong; Hurtig, Tomas; Pfaff, Sebastian; Zetterberg, Johan; Richter, Mattias; Kristensson, Elias; Ehn, Andreas

Published in:
Plasma Sources Science and Technology

DOI:
10.1088/1361-6595/abda9c

2021

Document Version:
Publisher's PDF, also known as Version of record

LETTER • **OPEN ACCESS**

Single-shot 3D imaging of hydroxyl radicals in the vicinity of a gliding arc discharge

To cite this article: Yupan Bao *et al* 2021 *Plasma Sources Sci. Technol.* **30** 04LT04

OPEN ACCESS
IOP Publishing

Letters
Plasma Sources Science and Technology

Plasma Sources Sci. Technol. **30** (2021) 04LT04 (7pp)
https://doi.org/10.1088/1361-6595/abda9c

Letter

Single-shot 3D imaging of hydroxyl radicals in the vicinity of a gliding arc discharge

Yupan Bao[1], Karolina Dorozynska[1], Panagiota Stamatoglou[1], Chengdong Kong[1,2], Tomas Hurtig[3], Sebastian Pfaff[1], Johan Zetterberg[1], Mattias Richter[1], Elias Kristensson[1] and Andreas Ehn[1,*]

[1] Department of Combustion Physics, Lund University, PO Box 118, S-221 00 Lund, Sweden
[2] Institute of Thermal Energy Engineering, School of Mechanical Engineering, Shanghai Jiao Tong University, Shanghai 200240, People's Republic of China
[3] Defence and Security, Systems and Technology, Swedish Defence Research Agency—FOI, SE 14725 Tumba, Stockholm, Sweden

E-mail: andreas.ehn@forbrf.lth.se

Received 18 June 2020, revised 18 November 2020
Accepted for publication 11 January 2021
Published 27 April 2021

Abstract

Plasma-related studies in gas phase are challenging to carry out due to plasma's transient and unpredictable behavior, excessive luminosity emission, 3D complexity and aggressive chemistry and physiochemical interactions that are easily affected by external probing. Laser-induced fluorescence is a robust technique for non-intrusive investigations of plasma-produced species. In this letter, we present 3D distributions of ground state hydroxyl radicals (OH) radicals in the vicinity of a glow-type gliding arc plasma. Such radical distributions are captured instantaneously in one single camera acquisition by combining structured laser illumination and a lock-in based imaging analysis method called FRAME. The interference of plasma emission is automatically subtracted by the FRAME technique. In addition, the orientation of the plasma discharge can be reconstructed from the 3D data matrix, which can then be used to calculate 2D distributions of ground state OH radicals in a plane perpendicular to the orientation of the plasma channel. Our results indicate that OH distributions around a gliding arc are strongly affected by gas dynamics. We believe that the ability to instantaneously capture 3D transient molecular distributions in a plasma discharge, with minimal plasma emission interference, will have a strong impact on the plasma community for *in situ* investigations of plasma-induced chemistry and physics.

Keywords: hydroxyl radicals, laser-induced fluorescence, three-dimensional molecular distribution, structured illumination, frequency recognition algorithm for multiple exposures

(Some figures may appear in colour only in the online journal)

Non-thermal plasma produced by gas discharges at atmospheric pressure generates high-energetic electrons with moderate gas heating (less than 2000 K). This feature, i.e. being able to efficiently enhance reactivity with low energy loss, makes non-thermal plasma a robust tool in many industrial applications [1]. The gliding arc discharge [2] is a

* Author to whom any correspondence should be addressed.

quasi-equilibrium plasma column that is ignited in the narrowest gap between two diverging electrodes in a gas flow. When generated, the plasma is close to thermal equilibrium but the gas temperature immediately starts falling to stabilize around 1000–2000 K while the electron temperature remains around 10 000 K (∼1 eV) [3, 4]. This feature is very attractive for efficiently enhancing chemical-reactivity as the high-temperature electrons generate reactive species, and up to 45% of the electrical energy could be directly absorbed in endothermic reactions [5]. Compared to other non-thermal sources, gliding arc discharges are widely used for their simplicity, economical accessibility and feasibility at atmospheric pressure.

Although the geometry and operation of the gliding arc discharge are simple, the plasma-induced physiochemical interactions with the ambient gas are complex and challenging to both model and investigate due to the transient dynamics, intricate physicochemical interactions and complex 3D-distributions of particles. Optical diagnostics have been applied to study gliding arc discharges at atmospheric pressure as they open up for *in situ* and non-intrusive investigation with outstanding temporal- and spatial resolution [3, 4, 6–9].

Hydroxyl radicals (OH) are generated from gliding arc discharges through electron-induced dissociation of water in ambient air [10, 11]. Ground state OH, in particular, is essential for plasma chemistry due to its high oxidation potential, especially for the decomposition of pollutant gases [4, 12–14]. Planar laser-induced fluorescence (PLIF) has previously been applied to observe ground state OH radicals produced in humid environments by discharges [12, 13]. A hollow structure of ground state OH in the near vicinity of a gliding arc discharge channel was observed and could be considered as a marker for the discharge channel [6, 15]. The central part of the area without an OH PLIF signal, from where plasma-emitted photons originate, contains electronically excited species, hot electrons and ions which basically is the plasma itself. The area just outside the plasma region contains ro-vibrationally excited species [16]. Both these areas will be further referred to as the non-thermal-equilibrium zone in this letter.

PLIF imaging generates a two-dimensional species distribution that is insufficient to fully describe the 3D feature of the gliding arc discharge and its surroundings. The surrounding at a certain point along the plasma discharge channel is ideally represented by a cylindrical coordinate system, $(\vec{h}, r, \theta)$, where $\vec{h}$ is the tangent of the plasma channel at this point and r and θ are cylindrical coordinates. The optical sampling system, however, is defined by a Cartesian coordinate system of the laser. Hence, a 2D representation from the PLIF data does not capture the full 3D description of the plasma discharge and it is thus not possible to render distributions of plasma-produced species in relation to the plasma channel.

There are two methods that are generally considered when 3D species distributions are needed: laser-based tomography [17] and segmentation PLIF [18]. Both methods require more than one camera acquisition, either by applying several cameras from different directions or a camera that can capture a series of images in a rapid sequence. Such experimental arrangements are both complex and rather specialized.

The current work utilizes structured illumination and a coded imaging analysis method called FRAME (frequency recognition algorithm for multiple exposures) [19] to capture instantaneous 3D ground-state OH-radical distributions around a gliding arc discharge using a standard ns-dye laser/ICCD camera setup. The FRAME method presented here can suppress plasma-light emission interferences and render 3D data matrices of laser-induced fluorescence from ground state OH. Information from such data is used here to study OH-distribution around the gliding arc discharge at different ambient conditions, capturing the complex 3D characteristic of the gliding arc.

The gliding arc discharge is driven by an AC power supply (Generator 9030E, 170 SOFTAL Electronic GmbH, Germany). It was set to run continuously at a frequency of 35 kHz, i.e. 28.6 μs per period, which yielded an input power of approximately 400 W for all three flow conditions applied in this investigation [20]. The two diverging electrodes were water-cooled stainless steel tubes with an outer diameter of 3 mm. An air jet is ejected from a 3 mm hole between the electrodes to force the plasma column to glide upwards along the electrodes. A more detailed sketch of the gliding arc system was presented by Kong *et al* [20].

A Nd:YAG pumped dye laser (Dye: Rhodamine 6G with ethanol, pulse energy: 40 mJ, pulse duration: 6 ns, repetition rate: 10 Hz) was used to generate UV laser light at 283.92 nm to excite ground state OH radicals ($A^2\Sigma^+ \xleftarrow[X^2]{} \Pi$ (1,0)). As shown in figure 1(a), the laser beam is split equally and shaped into four laser sheets that are spatially separated, 0.5 mm from each other, in the probe volume around 10 cm above the top of the electrodes. The intensity of each laser sheet is spatially modulated with sinusoidal patterns and enter the probe volume from different directions. The emitted fluorescence is directed by a mirror, placed above the probe volume, into an ICCD camera (Gen 2 Istar, 1024 × 1024 pixels, Andor Instruments). The camera is equipped with UV-transmissive optics (Nikkon UV 105 mm) and laser-induced fluorescence from all four laser sheets is captured in a single image acquisition. A Notch filter, centered at 310 nm ± 20 nm, is used to filter out scattered laser light and plasma emission. The gate width of the camera exposure time was set to 10 ns to mitigate most of the plasma emission and still capture the laser-induced signals.

The spatial modulation of the laser sheets is achieved by encoding a periodic intensity pattern into the laser sheet profile. The modulation scheme is graphically described in figure 1(b) where the light passes through a DOE (diffractive optical element, part number CU-281-Q-Y-A by HOLOOR) to be coded with a periodic pattern. Although the frequency pattern, generated by the DOE, is almost perfectly sinusoidal (87% in first orders), any existing overtones are removed by a spatial filter comprising of one cylindrical lens ($f = 750$ mm) and a spatial mask that only preserves the first order components in the focus. The laser sheet is created in a standard way where a second cylindrical lens ($f' = 1000$ mm) is used to form a thin laser sheet at a precise vertical location in the

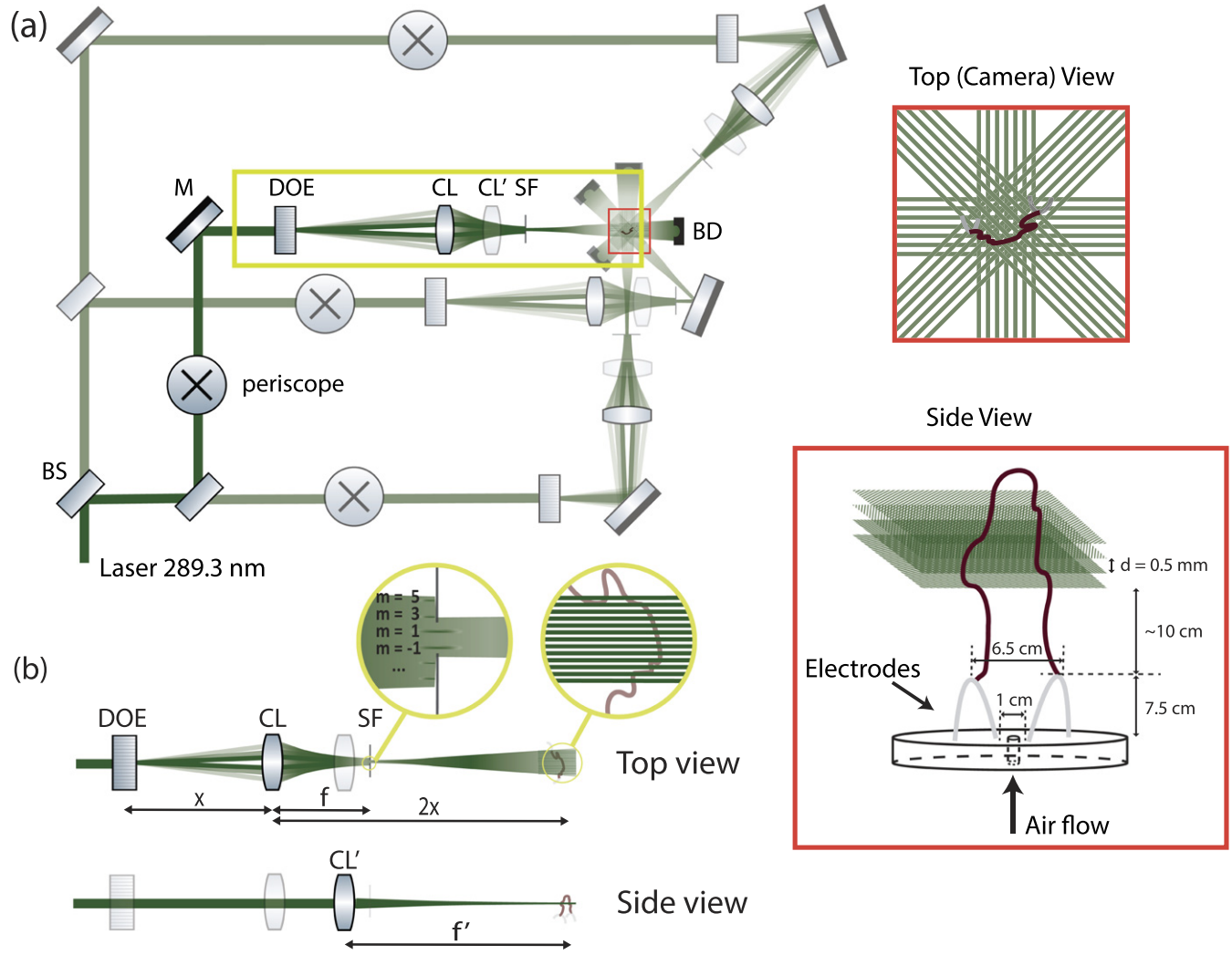

Figure 1. Optical arrangement for the experiment: BS- beam splitter, DOE- diffractive optical element, CL- vertically oriented cylindrical lens ($f = 750$ mm), CL- horizontally oriented cylindrical lens ($f' = 1500$ mm), SF- spatial filter, BD- beam dumps and d-separation distance between the laser sheets in the probe volume. (a) Overall view of the optical set-up with zoom-in top view and side view of the measurement volume shown on the right boxes. (b) The detailed optical arrangement of the modulated laser sheet creation [same as the yellow box in (a)]. The top view illustrates how the beam is horizontally modulated; the side view shows the creation of a conventional laser sheet vertically.

probe volume as shown in the side view of figure 1(b). A similar setup has been used and discussed in detail in previous publications from the group [21, 22]. The experimental arrangement, described above, can deliver four spatially modulated laser sheets into the experimental probe volume from four different directions. Each parallel layer of laser-excited OH radical distributions in the probe volume is hence tagged with a unique code that can be identified and extracted from the single acquisition using the analysis method FRAME [19]. Details about the imaging concept FRAME can be found in previous publications [21–23]. In this work, FRAME is later described through an example of a 3D reconstruction of OH in the vicinity of a gliding arc, displayed in figure 3.

An inherent benefit of the FRAME approach concerns suppression of light emission from plasmas. It is particularly challenging to distinguish OH PLIF from plasma emission when capturing laser-induced fluorescence from OH radicals at atmospheric conditions since a fair part of the plasma emission originates from plasma-related excitation of OH radicals. This challenge, however, is inherently minimized with structured illumination and FRAME analysis, as the background signal from the plasma emission does not have a coded structure, in contrast to the PLIF signal. Two cases where it is beneficial to remove the interfering plasma emission background are displayed in figure 2. The background signal is efficiently removed in both cases with a slight reduction in the spatial resolution providing nearly background-free PLIF images of ground state OH-radicals.

To render a 3D data matrix of ground state OH signal distributions with the FRAME approach, the first step is to apply a 2D Fourier transform on the raw data shown in figure 3(a). As a result of the different modulations of each laser sheet, the Fourier components of the modulated images are separated in the frequency domain as shown in figure 3(b). The four images with different modulations can be isolated and

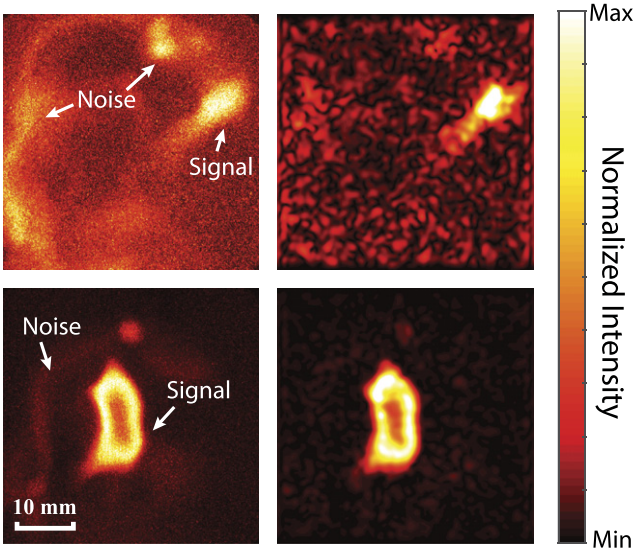

Figure 2. Plasma emission rejection using structured illumination and FRAME analysis. Two sets of raw (left) and processed (right) data with different signal to interference ratios (1:1 and 6:1) are demonstrated.

separately stored. This process is done by shifting the Fourier components of the image of interest to the origin and applying a Gaussian filter to remove all other modulated image components. Thereafter, the spatially resolved image can be extracted by an inverse Fourier transform. The four images, displayed in figure 3(c), are all extracted using this scheme and contain OH signal distributions from four layers in the probe volume.

A linear transition of the signal intensity between two neighboring layers is applied to generate a 3D reconstruction of the OH LIF signal. We believe that this 3D reconstruction scheme provides a high enough resolution to reproduce an accurate distribution of the ground state OH LIF signal since the distance between each laser sheet (0.5 mm) is shorter than the diameter of the non-thermal-equilibrium zone (∼5 mm as shown in figure 3(a)). Details of the 3D reconstruction process are described in [17].

The complex structure displayed in the upper part in figure 3(d) shows that the laser sheets are almost parallel to the plasma channel and it is therefore not possible to capture the full 3D OH-distribution around the gliding arc with the current setup. Moreover, the ring-like structure in the lower part of the 3D distribution is of particular interest as the orientation of its non-thermal-equilibrium zone displays the direction of the local plasma channel. This orientation can be calculated and utilized to achieve 2D OH-LIF distributions perpendicular to the direction of the plasma channel.

The orientation of the plasma channel is estimated by locating the non-thermal-equilibrium zones in the four image planes. The locations of the four non-thermal-equilibrium zones are defined by their center-of-mass and the orientation is found by a 3D linear fit to these positions. This orientation, in relation to the laser sheets, is shown by the blue $\vec{h}$-vector in figure 4(a). The angle α between $\vec{h}$ and the planar laser sheets, i.e. x–y plane in figure 4(a), is calculated to be 57°. The angle would be 90° if the plasma channel were perpendicular to the laser sheets. This result shows that OH PLIF data suffers from 3D effects even though the ring-like structure displays a fairly symmetric shape. Among the 64 ring-like OH structures analyzed, the smallest α is 18°, which indicates that the actual OH distribution could be 3 times [$\sin(18°) = 0.31$] wider in one direction compared to what is shown in a 2D PLIF image. Therefore, the 3D-effects on OH signal distributions are not easily observable in 2D PLIF images and it may cause severe misinterpretations of the data.

Distributions of ground state OH, free from 3D-effect, can be represented in the discharge coordinate system, ($\vec{h}$, r, θ), and show data perpendicular to the orientation of the plasma channel. Two approaches to achieve such distributions are here described. The first approach is to extract the 2D distribution of OH, perpendicular to the plasma channel ($\vec{h}$), directly from the 3D data matrix of the probe volume. Five such images (slices), obtained at different heights (h) along the $\vec{h}$-axis, are presented in figure 4(a). It is noticeable that the area of the image that contains signal is smaller compared to the 2D PLIF images and the position of the signal-contained area changes with h. This is a consequence of the small α angle where only a part of the OH-signal is included in the perpendicular slices at a certain height (h).

The drawback, however, could be circumvented by employing a second method where the whole ring-like structure can be viewed in one image. Since the distance between each laser sheet (0.5 mm) is much smaller than the observed diameter (2–5 mm) of the OH PLIF signal around the discharge [8], it is reasonable to assume that the OH distribution along $\vec{h}$ is close to homogeneous between h_1 and h_2 as shown in the sketch in figure 4(b). Therefore, the 3D-effects could be removed by projecting one of the reconstructed images sections, shown in figure 3(c), onto the plane that is perpendicular to $\vec{h}$ as shown in figure 4(b).

Using the second approach, the area of the non-thermal-equilibrium zone and the OH ring can be analyzed quantitatively. The OH ring is defined as the area containing both ground state OH and the non-thermal-equilibrium zone. Due to the circular shape of the non-thermal-equilibrium zone and the OH ring, the areas are characterized by their effective diameters, d and D, respectively. The effective diameters of 39 OH rings (D) and 55 non-thermal-equilibrium zones (d) are plotted in figure 5(a) for three flow conditions, 10, 15 and 20 l min^{-1}, where both D and d decreases with higher flow rate. This observation is consistent with our previous result reported by Zhu *et al* [6] that the ground state OH distribution around the gliding arc discharge, i.e. D, is reduced in size with an increased flow rate. Here we confirm that the structure inside the OH distribution, i.e. d, also shrinks with a higher flow rate. In addition, the two gliding arc discharges, used in [6] for comparison, were of two different types: a glow-type for the low flow rate (17.5 l min^{-1}), and a spark-type for the high flow rate (42 l min^{-1}). In this work, however, the gliding arc discharge remains glow-type for all the three investigated flow conditions. The size of the OH distribution (D) should be strongly related to the amount of energy that is deposited into the gas by the gliding arc. The energy deposition will form charged, excited and reactive species as well as heat up ambient gas. A

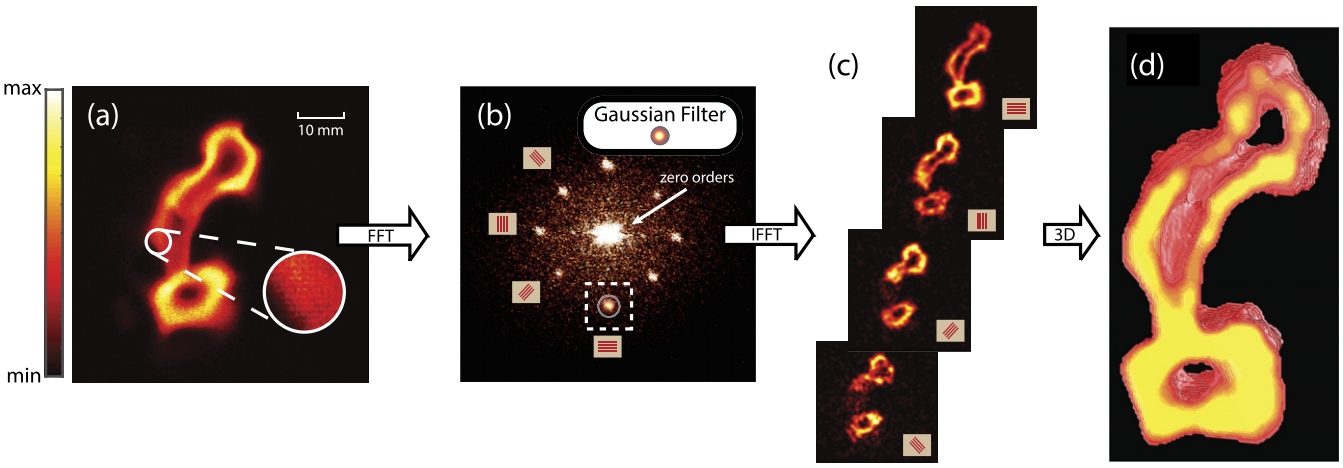

Figure 3. Reconstruction of OH around a gliding arc. (a) Raw data of a quadruple exposed OH PLIF signal from the four image layers. Modulations from different laser sheets are seen in the magnified area. (b) The Fourier transform of the raw data with the signs near the first order signals represent the spatial modulation of the laser beam. An example of how a Gaussian filter is applied on the signal is given in the white dashed box. (c) Inverse Fourier transform of each modulation from (b). The position of the images (from the top to bottom) corresponds to positions of the four laser sheets illuminating the target. (d) The 3D reconstruction of the OH signal.

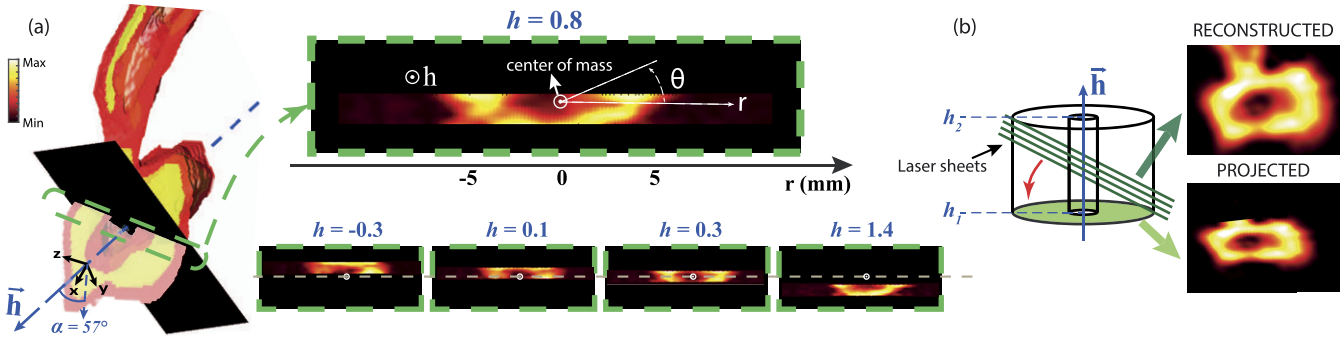

Figure 4. Three-dimensional-effects free OH distribution obtained from (a) a cross-section of the plane perpendicular to $\vec{h}$ and the 3D data matrix and (b) a projection of one of the reconstructed images of the perpendicular plane. The blue vector $\vec{h}$ is the orientation of the discharge estimated by the center-of-mass of the non-thermal-equilibrium zone from the four reconstructed images. (a) Discharge coordinate system, ($\vec{h}$, r, θ), can be used for the 3D-effects-free images as shown in the top green dashed box. As a result of the non-90° angle of α, a shift of the signal-contained area in slices obtained at different heights h is observed as shown in the four small green dashed boxes. (b) A sketch of the OH distribution around a gliding arc and the laser sheets is shown on the left. The ring-like structure of OH distribution is preserved in the 3D-effects-free image obtained by direct projection (on the right). The same data is used here as in figure 3.

hot shielding gas layer will form around the plasma channel and the layer will, with time, expand since more gas will be heated and the gas temperature will increase. For higher flow rates, re-ignition takes place more frequently and the maximum length of a conducting channel is shorter [6]. As a result, there is less time for the hot shielding gas to be developed with a higher flow rate. Thus the size of D and d will be smaller as shown in figure 5(a).

Re-ignition occurs when the impedance in the gliding arc channel causes the applied voltage to become high enough so that a new discharge channel is formed at the narrowest gap between the electrodes (as presented in figure 4 of reference [6]). It is clear from these processed images, free from 3D-effects, that the OH-distribution around the gliding arc is non-circular. This non-circular distribution indicates that the plasma-processed environment is strongly affected by the gas flow. Distortion of the shielding layer would increase the impedance in the gliding arc discharge that, in turn, could trigger re-ignition. In addition, when two OH rings merge together, the local impedance between these structures will decrease, increasing the likelihood for short-cuttings. The total impedance of the gliding arc will be lowered after short-cuttings. Thus frequent short-cutting lowers the possibility of re-ignition. As the diameter of the OH rings, i.e. D, is smaller with a higher flow rate and the likelihood for short-cuttings will be lower. Consequently, the possibility of re-ignition for the higher flow rate will be higher, which is consistent with the results reported in [6].

The relation between D and d, analyzed from 36 separate ring-like structures, are plotted in figure 5(b) with linear fit and a 95% prediction interval. The gradient of the linear fit decreases with higher flow rates, which means that the relative shrinking behavior of D is larger than d when the flow increases. This result indicates that the ground state OH acts

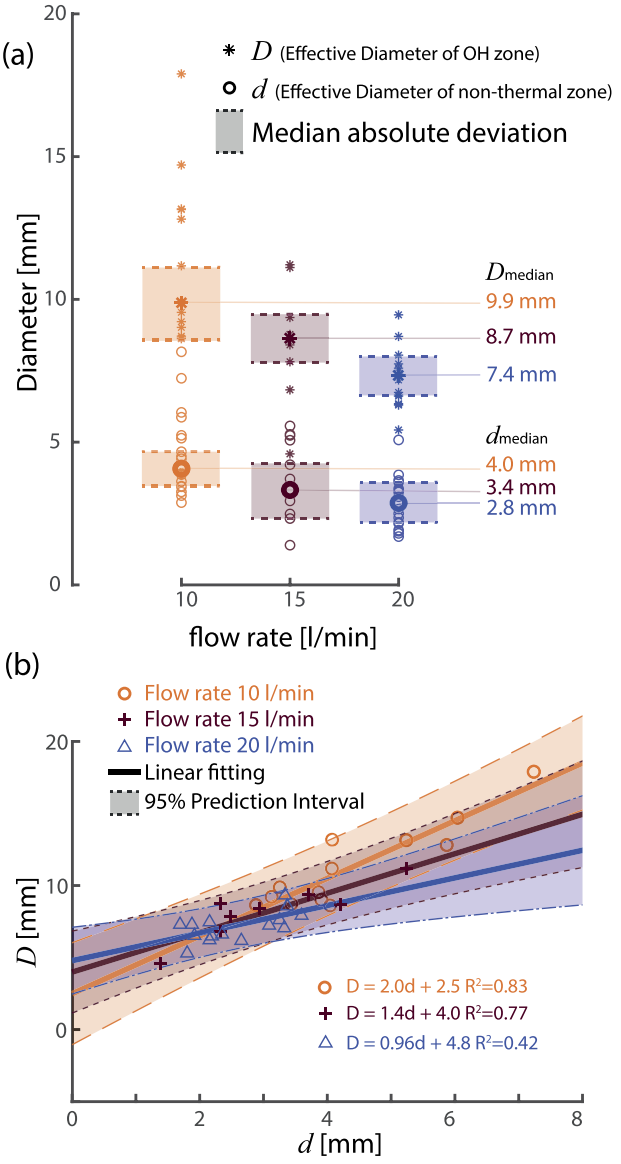

Figure 5. (a) The effective diameters of 39 OH rings (D) and 55 non-thermal-equilibrium zones (d) at different flow rate conditions. (b) Linear fit of D and d at different flow rate conditions.

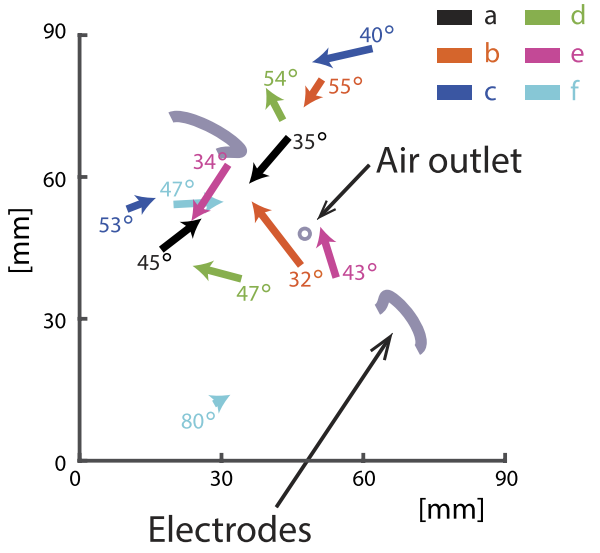

Figure 6. The orientations of discharge channels calculated from 6 pairs (as 6 different colors) of ring-like OH distributions in respect of the position of the electrodes and air outlet. The angle α of each orientation is noted around the vector with the same color. A longer length of the orientation vector indicates a smaller α.

like a protecting layer for the non-thermal-equilibrium zone from the flow influence.

The orientation of discharge channels, captured 10 cm above the electrodes, are displayed in figure 6. These particular datasets contain OH distributions from a gliding arc that crosses the laser sheets twice, showing a pair of ring-like structures. The orientation of the plasma channel, at the two crossing points, can be pointing towards each other as shown by pair a, b and c, diverging as pair d and e or nearly parallel to each other as pair f. The orientation from a pair of crossing points, for one gliding arc channel, seems to be non-correlated to each other. The unpredictable and randomized orientation and the transient behavior of the gliding arc channel, clearly show the challenge of studying the physics and chemistry in the vicinity of a discharge channel, especially when limited to conventional 2D PLIF. Furthermore, the angle α, shown in figure 6, is ranging from 32° to 80°. Being able to capture OH-distribution data that can be corrected for 3D-effects in such wide angles shows how versatile this method is for studying species specific distributions in the vicinity of a plasma discharge.

In summary, we have combined PLIF of ground state OH radicals with structured illumination and FRAME analysis to achieve (1) plasma-emission background rejection and (2) reconstruction of 3D distributions of ground state OH radicals around a plasma discharge using a standard Nd:YAG-Dye laser system and an ICCD camera. We have further demonstrated that the 3D data matrix can be utilized to identify and compensate for 3D-effects that arise due to the complex 3D structure of the discharge channel. Based on this method, the effective diameters of the non-thermal-equilibrium zone and the OH ring have been quantitatively analyzed. The presented data shows that both these geometries, D and d, are strongly affected by gas dynamics.

Experimental investigations and analysis of transient and stochastic plasma discharges are well-known challenges in the plasma community, both in studies of fundamental plasma properties and plasma applications. We believe that the sets of novel methods presented here will have a major impact in future plasma-related research.

Acknowledgments

This work was financially supported by the Swedish Energy Agency, the Swedish Research Council, the Knut and Alice Wallenberg Foundation and the European Research Council.

ORCID iDs

Yupan Bao https://orcid.org/0000-0001-8386-7109

Karolina Dorozynska https://orcid.org/0000-0002-3702-1513
Panagiota Stamatoglou https://orcid.org/0000-0003-0732-3382
Chengdong Kong https://orcid.org/0000-0003-3713-0653
Sebastian Pfaff https://orcid.org/0000-0002-8528-9362

References

[1] Roth J R 2001 *Industrial Plasma Engineering: volume 2: Applications to Nonthermal Plasma Processing* vol 2 (Boca Raton, FL: CRC press)
[2] Fridman A, Nester S, Kennedy L A, Saveliev A and Mutaf-Yardimci O 1999 *Prog. Energy Combust. Sci.* **25** 211–31
[3] Czernichowski A, Nassar H, Ranaivosoloarimanana A, Fridman A A, Simek M, Musiol K, Pawelec E and Dittrichova L 1996 *Acta Phys. Pol.* A **89** 595–603
[4] Zhu J, Ehn A, Gao J, Kong C, Aldén M, Salewski M, Leipold F, Kusano Y and Li Z 2017 *Opt. Express* **25** 20243–57
[5] Czernichowski A 1994 *Pure Appl. Chem.* **66** 1301–10
[6] Zhu J, Sun Z, Li Z, Ehn A, Aldén M, Salewski M, Leipold F and Kusano Y 2014 *J. Phys. D: Appl. Phys.* **47** 295203
[7] Gao J, Zhu J, Ehn A, Aldén M and Li Z 2016 *Plasma Chem. Plasma Process.* **37** 433–50
[8] Zhu J, Kusano Y and Li Z 2016 *Atmospheric Pressure Plasmas: Processes, Technology and Applications* (New York: Nova Science Publishers)
[9] Zhu J *et al* 2015 *Appl. Phys. Lett.* **106** 044101
[10] Itikawa Y and Mason N 2005 *J. Phys. Chem. Ref. Data* **34** 1–22
[11] Dolan T J 1993 *J. Phys. D: Appl. Phys.* **26** 4
[12] Kanazawa S, Kawano H, Watanabe S, Furuki T, Akamine S, Ichiki R, Ohkubo T, Kocik M and Mizeraczyk J 2011 *Plasma Sources Sci. Technol.* **20** 034010
[13] Ono R and Oda T 2001 *IEEE Trans. Ind. Appl.* **37** 709–14
[14] Zhu F, Li X, Zhang H, Wu A, Yan J, Ni M, Zhang H and Buekens A 2016 *Fuel* **176** 78–85
[15] Gao J, Kong C, Zhu J, Ehn A, Hurtig T, Tang Y, Chen S, Aldén M and Li Z 2019 *Proc. Combust. Inst.* **37** 5629–36
[16] Raizer Y P and Allen J E 1997 *Gas Discharge Physics* vol 2 (Berlin: Springer)
[17] Nygren J, Hult J, Richter M, Aldén M, Christensen M, Hultqvist A and Johansson B 2002 *Proc. Combust. Inst.* **29** 679–85
[18] Halls B R, Thul D J, Michaelis D, Roy S, Meyer T R and Gord J R 2016 *Opt. Express* **24** 10040–9
[19] Ehn A, Bood J, Li Z, Berrocal E, Aldén M and Kristensson E 2017 *Light Sci. Appl.* **6** e17045
[20] Kong C, Gao J, Zhu J, Ehn A, Aldén M and Li Z 2018 *J. Appl. Phys.* **123** 223302
[21] Li Z, Borggren J, Berrocal E, Ehn A, Aldén M, Richter M and Kristensson E 2018 *Combust. Flame* **192** 160–9
[22] Kristensson E, Li Z, Berrocal E, Richter M and Aldén M 2017 *Proc. Combust. Inst.* **36** 4585–91
[23] Dorozynska K and Kristensson E 2017 *Opt. Express* **25** 17211–26